Journal of Computational Physics 229 (2010) 7238–7259

Contents lists available at ScienceDirect

Journal of Computational Physics

journal homepage: www.elsevier.com/locate/jcp

Simulation of surface tension in 2D and 3D with smoothed particle hydrodynamics method

Mingyu Zhang *

Institute of Applied Physics and Computational Mathematics, Beijing 100094, China

ARTICLE INFO

Article history:
Received 12 October 2009
Received in revised form 13 May 2010
Accepted 7 June 2010
Available online 23 June 2010

Keywords:
Surface tension
Interfacial flow
Smoothed particle hydrodynamics
Moving least squares method

ABSTRACT

The methods for simulating surface tension with smoothed particle hydrodynamics (SPH) method in two dimensions and three dimensions are developed. In 2D surface tension model, the SPH particle on the boundary in 2D is detected dynamically according to the algorithm developed by Dilts [G.A. Dilts, Moving least-squares particle hydrodynamics II: conservation and boundaries, International Journal for Numerical Methods in Engineering 48 (2000) 1503–1524]. The boundary curve in 2D is reconstructed locally with Lagrangian interpolation polynomial. In 3D surface tension model, the SPH particle on the boundary in 3D is detected dynamically according to the algorithm developed by Haque and Dilts [A. Haque, G.A. Dilts, Three-dimensional boundary detection for particle methods, Journal of Computational Physics 226 (2007) 1710–1730]. The boundary surface in 3D is reconstructed locally with moving least squares (MLS) method. By transforming the coordinate system, it is guaranteed that the interface function is one-valued in the local coordinate system. The normal vector and curvature of the boundary surface are calculated according to the reconstructed boundary surface and then surface tension force can be calculated. Surface tension force acts only on the boundary particle. Density correction is applied to the boundary particle in order to remove the boundary inconsistency. The surface tension models in 2D and 3D have been applied to benchmark tests for surface tension. The ability of the current method applying to the simulation of surface tension in 2D and 3D is proved.

1. Introduction

Surface tension has a significant influence on the fluid flow with free surface or multi-phase flow with a sharp interface, such as a breaking dam, capillarity, binary coalescence. Surface tension force acts on the interface and the interface tends to become as small as possible [1]. Applications in natural phenomena and industrial processes, such as water beading on a leaf, water dripping from a tap, formation of soap bubbles, ink-jet printing, thermal spray coating involves with effects of surface tension at the liquid–liquid interface.

Many meshed methods have been applied to investigate the fluid flow with surface tension. Brackbill et al. [2] presented the continuum surface force (CSF) method to model the surface tension. In general, the CSF model is applicable to fluid flow dominated by interfacial surface tension. It has been applied to investigate incompressible fluid flow in low gravity environments, capillarity, and droplet dynamics. Sussman et al. [3] developed a level set approach for incompressible two phase flow with surface tension. The new treatment of level set method can be applied to the problem with large density and viscosity

* Tel.: +86 10 59872029.
E-mail address: zhang_mingyu@iapcm.ac.cn

0021-9991/$ - see front matter © 2010 Elsevier Inc. All rights reserved.
doi:10.1016/j.jcp.2010.06.010

ratio. And the motion of air bubbles in water and falling water drops in air are investigated in the work. Chang et al. [4] derived a level set formulation for incompressible, immiscible Navier–Stokes equations separated by a free surface. These methods are robust and efficient and are capable of computing interface singularities such as merging and reconnection. Bussman et al. [5,6] developed a three-dimensional volume tracking model of droplet impact. Surface tension is modeled as a volume force acting on fluid near the free surface. The fingering and splashing of a droplet impacting a solid surface is investigated numerically.

Meshless methods such as SPH method [7–9] has been applied to simulate the fluid flow with free surface. Nugent and Posch [10] first developed a SPH model for surface tension. The cohesive pressure of the van der Waals (vdW) model gives rise to an attractive, central force between the particles with an interaction range. The oscillation of deformed drop is studied with the SPH model. Meleán et al. [11,12] applied the vdW model to simulate the oscillation of the deformed drop without tensile instability. Later, it is extended to the numerical investigation of head-on and off-center binary collision. And López and Sigalotti [13] used the vdW model to investigate the oscillation of elliptic drop. Colagrossi and Landrini [14] present a SPH formulation for two-dimensional interfacial flows. The formulation remains stable for the low density ratios. Tartakovsky and Meakin [15,16] presented a surface tension model to simulate unsaturated flow through fracture junctions, the classical two-dimensional Rayleigh–Taylor instability and three-dimensional miscible flow in fracture apertures with complex geometries. All the above methods give very good results. However, the surface tension force is not set explicitly. And there are artificial coefficients in these methods and the choice of the artificial coefficient is arbitrary. The surface tension force has to be calibrated by using the Laplace's formulation. And also the initial temperature has to be chosen specifically for the vdW model. It undermines the application of the vdW model to free surface problem related to heat transfer. Morris [17] developed the SPH formulation for the CSF model. The interface is tracked implicitly by simulating the advection of the color function. The method suffers from difficulty of accurate representation of interface curvature. Hu and Adams [18–20] presented an CSF model for the SPH method and applied it into the incompressible multi-phase flow. The incompressible multi-phase SPH method works well and gives excellent results in the simulation of droplet oscillation, contact angle, droplet deformation in shear flow, Rayleigh–Taylor instability. The method has high computational efficiency and has been extended to the simulation of flows with high density ratio.

In this paper, the methods for simulating surface tension with SPH method in two dimensions and three dimensions are developed. In 2D surface tension model, the boundary particles are detected dynamically by using the algorithm developed by Dilts [21] and the interface is reconstructed locally by using Lagrangian interpolation polynomial. In 3D surface tension model, the boundary particles are tracked explicitly by using the algorithm developed by Haque and Dilts [22] and the boundary surface is reconstructed locally by using MLS. The curvature and normal vector are calculated according to the reconstructed interface and then surface tension force can be obtained. Surface tension force acts only on the boundary particles. In order to remove the boundary inconsistency, density correction is applied on the boundary particles. The details of the method are given in the next sections.

2. Numerical model

SPH is a meshless Lagrangian method for fluid dynamics simulation. As a particle method, SPH uses a set of particles to represent fluid flow [8]. And the approximate numerical solutions of the equations of fluid dynamics are calculated on these particles. Mathematically, the particles are only the interpolation points. SPH is a popular and attractive method in the field of computational fluid dynamics in the past twenty years. Although SPH is still in the state of development, improvements of the stability, consistence, and convergence for the SPH have been obtained because of the continuous endeavor of many science researchers. The standard SPH will be given in the following.

The mass density ρ_i of particle at position $\vec{x}_i$ can be evaluated by using the summation density:

$$\rho_i(\vec{x}) = \sum_{j=1}^{N} m_j W_{ij} \tag{1}$$

where $W_{ij} = W(\vec{x}_{ij}, h)$ is the smoothing function, and $\vec{x}_{ij} = \vec{x}_i - \vec{x}_j$, m_i denotes the mass of particle i, h represents the smoothing length and $\vec{x}_i$ is the position of particle i. By integrating Eq. (1), we obtain the total mass of the system which is equal to the summation of all the particles. The summation density has the property of mass conservation. To reduce the particle deficiency on the boundary, the summation density is normalized on the boundary as below [23]

$$\rho_i(\vec{x}) = \frac{\sum_{j=1}^{N} m_j W_{ij}}{\sum_{j=1}^{N} \left(\frac{m_j}{\rho_j}\right) W_{ij}}. \tag{2}$$

Applying the SPH particle approximation to the Lagrangian form of Navier–Stokes equations, a symmetric form is obtained to preserve variational consistency. The momentum equation can be written as follows:

$$\frac{D\vec{v}_i}{Dt} = -\sum_{j=1}^{N} m_j \left(\frac{p_i}{\rho_i^2} + \frac{p_j}{\rho_j^2}\right) \nabla_i W_{ij} + \sum_{j=1}^{N} m_j \left(\frac{\tau_i}{\rho_i^2} + \frac{\tau_j}{\rho_j^2}\right) \cdot \nabla_i W_{ij} + \frac{1}{\rho_i} \vec{f}. \tag{3}$$

The RHS of Eq. (3) consists of the pressure, viscous force and surface tension force. XSPH [24] is used in the calculation and the velocity is revised by

$$\frac{d\vec{x}_i}{dt} = \vec{v}_i - \varepsilon \sum_j \frac{m_j}{\rho_j} \vec{v}_{ij} W_{ij}, \tag{4}$$

where $\vec{v}_{ij} = \vec{v}_i - \vec{v}_j$ and ε is a constant ranging from 0 to 1. XSPH makes the SPH particles moving more orderly. The pressure is calculated according to the equation of the state as below

$$p = c^2(\rho - \rho_0), \tag{5}$$

where ρ_0 is the reference density of fluid and c is the speed of sound. The particle approximation for the viscous stress tensor τ is [25]

$$\tau_i = -\sum_{j=1}^{N} \frac{m_j}{\rho_j} \mu_i \vec{v}_{ij} \nabla_i W_{ij} - \sum_{j=1}^{N} \frac{m_j}{\rho_j} \mu_i (\nabla_i W_{ij}) \vec{v}_{ij} + \left(\frac{2}{3} \sum_{j=1}^{N} \frac{m_j}{\rho_j} \mu_i \vec{v}_{ij} \cdot \nabla_i W_{ij} \right) I. \tag{6}$$

The surface tension force is calculated as below [2,17]

$$\vec{f} = \sigma \kappa \vec{n} \delta_\varepsilon, \tag{7}$$

where the σ is the coefficient of surface tension, κ is the curvature of surface, $\vec{n}$ is the normal vector of surface and δ_ε is the surface delta function. δ_ε is simply set to a constant $1/\varepsilon$ on the interface. And ε takes the value of the particle spacing. The surface gradient term is not considered here, since the coefficient of surface tension is assumed to be constant.

In order to obtain surface tension force acting on the boundary particle, the SPH particles on the interface are detected dynamically and the interface curve is reconstructed locally in the transformed coordinate by using Lagrangian interpolation method in 2D and by MSL in 3D, respectively. Then the curvature and normal vector of the interface are obtained according to the reconstructed interface. The detailed algorithms are given in the following.

2.1. 2D Surface tension model

2.1.1. Boundary particle detection in 2D

Based on the technique developed by Dilts [21], the boundary particle in 2D is detected by scanning the κh-diameter (κh is the dimension of the support domain) circle around an SPH particle. If the circle of an SPH particle is not completely covered by the circles of its neighbors, the SPH particle is a boundary particle. Otherwise, it is an inner particle. In the current algorithm, the arc checking method is applied to scan the κh-diameter circle coverage. The range of the circle is set to be $[0, 2\pi)$. The covered arcs are represented by a set of angle interval $[\alpha_1, \alpha_2]$. The circle of particle i is covered only if the following condition is satisfied

$$\bigcup_j [\alpha_1, \alpha_2] = [0, 2\pi), \tag{8}$$

where j is the particle index of neighbors of particle i. The details for the boundary particle detection in 2D can be found in Ref. [21].

2.1.2. Reconstruction of the interface curve in 2D

The interface curve is reconstructed on the boundary particle. Before the reconstruction of the interface curve, the coordinate system is transformed to local coordinate system as shown in Fig. 1. The advantage of transformation of the coordinate system is that the interface curve is guaranteed to be one-valued in the local coordinate system. For boundary particle i, the local coordinate origin O' is the average point of the neighbors of the boundary particle i. The coordinate of point O' are given as the following:

$$x_{O'} = \sum_j x_j \Big/ N_i, \tag{9}$$

$$y_{O'} = \sum_j y_j \Big/ N_i, \tag{10}$$

where j is the particle index of neighbors of boundary particle i and N_i is total number of neighbors of boundary particle i. The direction of the y' axis is the same as that of the straight line from the local coordinate origin O' to boundary particle i. The x' axis is perpendicular to the y' axis. The rotation angle α of the local coordinate system, i.e. the angle between x axis in the original coordinate system and x' axis in the local coordinate system, is given by

$$\alpha = \begin{cases} 2\pi - \cos^{-1}(r_y/r) & \text{if } r_x > 0, \\ \cos^{-1}(r_y/r) & \text{if } r_x \leqslant 0, \end{cases} \tag{11}$$

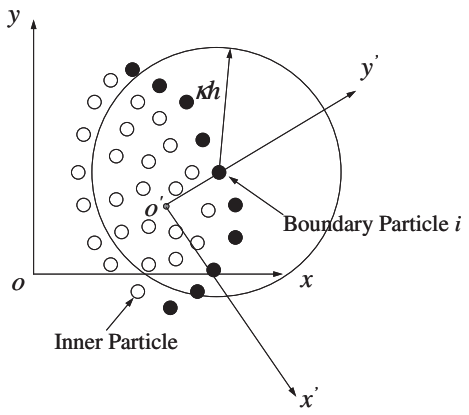

Fig. 1. Transformation of the coordinate system based on the average point O' of the neighbors of boundary particle i in 2D.

where

$$r_x = x_i - x_{O'}, \tag{12}$$

$$r_y = y_i - y_{O'}. \tag{13}$$

x_i and y_i is the coordinate of particle i in the x and y direction, respectively. The relationship between the local coordinate and the original coordinate is given by

$$x' = x\cos\alpha + y\sin\alpha, \tag{14}$$

$$y' = -x\sin\alpha + y\cos\alpha. \tag{15}$$

The interface curve is reconstructed locally on boundary particle i and its neighbors. It is guaranteed that the interface reconstructed locally is one-valued in the local coordinate system. The Lagrangian interpolation polynomial is used to fit the interface curve in the local coordinate system. The Lagrangian interpolation polynomial is given by

$$P(x) = \sum_j P_j(x), \tag{16}$$

where

$$P_j(x) = y_j \prod_{k\neq j} \frac{(x - x_k)}{(x_j - x_k)}. \tag{17}$$

j is particle index including boundary particle i and its neighbors on the boundary. For simplicity, the prime of the local coordinate is neglected. The coordinate in the Lagrangian interpolation polynomial and its derivative is in the local coordinate system.

2.1.3. Curvature and normal vector of the interface in 2D

The curvature and normal vector of the interface are calculated from the reconstructed curve. The curvature κ is given by

$$\kappa = \frac{|P''(x)|}{[1 + P'^2(x)]^{3/2}}, \tag{18}$$

where $P'(x)$ and $P''(x)$ are the first and second derivative of interface function $P(x)$, respectively.

Since the surface tension force is towards the fluid for convex interface and outwards the fluid for concave interface, the direction of surface tension force should be specified according to the second derivative of the interface curve. The direction of normal vector of the interface is set to be the same as the direction of surface tension force. The normal vector of the interface $\vec{n}'$ in the local coordinate system (as shown in Fig. 2) is taken as

$$\vec{n}' = \begin{cases} \langle P'(x), -1\rangle & \text{if } P''(x) < 0, \\ \langle -P'(x), 1\rangle & \text{if } P''(x) > 0. \end{cases} \tag{19}$$

The normal vector of the interface calculated by Eq. (19) should be transformed to normal vector in the original coordinate system by rotating. Finally the normal vector of the interface $\vec{n}$ is given as

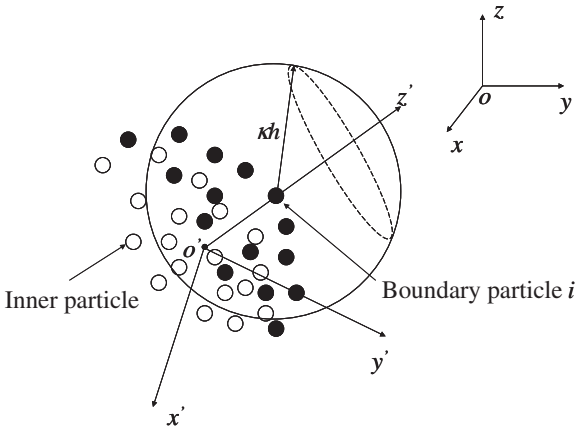

Fig. 2. Transformation of the coordinate system based on the average point O' of the neighbors of boundary particle i in 3D.

$$\vec{n} = \begin{cases} \langle P'(x)\cos\alpha + \sin\alpha, P'(x)\sin\alpha - \cos\alpha\rangle & \text{if } P''(x) < 0, \\ \langle -P'(x)\cos\alpha - \sin\alpha, -P'(x)\sin\alpha + \cos\alpha\rangle & \text{if } P''(x) > 0, \end{cases} \tag{20}$$

where α is the rotation angle from the original coordinate system to the local coordinate system. The curvature will not change with the transformation of the coordinate system.

The curvature and normal vector of the interface are given by Eqs. (18) and (20), respectively. The surface tension force can be calculated by Eq. (7).

2.2. 3D Surface tension model

2.2.1. Boundary particle detection in 3D

Based on the method developed by Haque and Dilts [22], the SPH particles on the boundary surface in 3D are detected dynamically by checking the coverage of the sphere of radius d_i (the dimension of the support domain) centered at particle i. The algorithm of the coverage of the sphere is given as below. The sphere with the radius of the dimension of the support domain is created for each SPH particle. The surface circles on the candidate boundary sphere are obtained by the interactions with the neighbor spheres. The coverage of all the surface circles on the boundary sphere is checked by using the two-dimensional algorithm developed by Dilts [21]. If any of the surface circles is not completely covered, the candidate SPH particle is on the boundary. Otherwise, the SPH particle is an inner particle. The details of the 3D boundary detection method can be found in Ref. [22].

2.2.2. Reconstruction of the interface in 3D

The boundary particles in 3D are detected, and then the boundary surface can be reconstructed based on MLS. Before the reconstruction of the boundary surface, the coordinate system is transformed to local coordinate system as shown in Fig. 2. The advantage of the transformation of the coordinate system is that the boundary surface is guaranteed to be one-valued in the local coordinate system. For boundary particle i, the local coordinate origin O' is the average point of the neighbors of boundary particle i. The coordinate of point O' are given as the following:

$$x_{O'} = \sum_j x_j \Big/ N_i, \tag{21}$$

$$y_{O'} = \sum_j y_j \Big/ N_i, \tag{22}$$

$$z_{O'} = \sum_j z_j \Big/ N_i, \tag{23}$$

where j is the particle index of neighbors of boundary particle i and N_i is total number of the neighbors of boundary particle i. The direction of the z' axis is that of radial from the local coordinate origin O' to boundary particle i. The $x'y'$ plane is perpendicular to z' axis. The directions of x', y' and the z' axis is given by

$$\hat{\vec{z}}_{ij} = \frac{\langle x_i - x_{O'}, y_i - y_{O'}, z_i - z_{O'}\rangle}{\left[(x_i - x_{O'})^2 + (y_i - y_{O'})^2 + (z_i - z_{O'})^2\right]^{\frac{1}{2}}}, \tag{24}$$

$$\hat{\vec{x}}_{ij} = \begin{cases} \frac{\hat{\vec{x}}\times\hat{\vec{z}}_{ij}}{\left\|\hat{\vec{x}}\times\hat{\vec{z}}_{ij}\right\|} & \text{if} \quad \hat{\vec{y}}\times\hat{\vec{z}}_{ij} = 0, \\ \frac{\hat{\vec{y}}\times\hat{\vec{z}}_{ij}}{\left\|\hat{\vec{y}}\times\hat{\vec{z}}_{ij}\right\|} & \text{if} \quad \hat{\vec{y}}\times\hat{\vec{z}}_{ij} \neq 0, \end{cases} \tag{25}$$

$$\hat{\vec{y}}_{ij} = \frac{\hat{\vec{z}}_{ij}\times\hat{\vec{x}}_{ij}}{\left\|\hat{\vec{z}}_{ij}\times\hat{\vec{x}}_{ij}\right\|}, \tag{26}$$

where $\hat{\vec{x}}_{ij}$, $\hat{\vec{y}}_{ij}$, and $\hat{\vec{z}}_{ij}$ are the unit vectors in x, y, and z axis of the local coordinate system, respectively. $\hat{\vec{x}}$ and $\hat{\vec{y}}$ are the unit vectors in the x and y axis of the original coordinate system, respectively. The relationship between the local coordinate (x',y',z') and the original coordinate (x,y,z) is given by

$$x' = \langle x,y,z\rangle \cdot \hat{\vec{x}}_{ij}, \tag{27}$$

$$y' = \langle x,y,z\rangle \cdot \hat{\vec{y}}_{ij}, \tag{28}$$

$$z' = \langle x,y,z\rangle \cdot \hat{\vec{z}}_{ij}. \tag{29}$$

In the transformed coordinate system, the boundary surface is reconstructed by using the MLS. The MLS is a useful method to reconstruct the 3D surface from a set of points. Since the second derivatives of the surface function should be given in the calculation, the quadratic basis is used in the MLS. The quadratic basis is given as below

$$p^T = [1, x, y, x^2, xy, y^2]. \tag{30}$$

According to the definition from Lancaster and Salkauskas [26], the surface function (the coordinate in the z direction of the particle on the boundary surface) can be approximated as

$$z^h(\vec{x}) = \sum_{i=1}^{m} p_i\left(\vec{\vec{x}}\right) a_i(\vec{x}) \equiv p^T\left(\vec{\vec{x}}\right)\cdot a(\vec{x}), \tag{31}$$

where m is the number of terms in the basis and

$$a(\vec{x}) = [a_1(\vec{x}), a_2(\vec{x}) \cdots a_m(\vec{x})]. \tag{32}$$

The coefficients a is chosen to minimize

$$J = \sum_I w(\vec{x}-\vec{x}_I)(z^h(\vec{x},\vec{x}_I) - z(\vec{x}_I))^2 = (Pa-z)^T W(\vec{x})(Pa-z), \tag{33}$$

where $w(\vec{x}-\vec{x}_I)$ is the weighting function which is the same as that used in SPH,

$$z^T = (z_1, z_2, \ldots, z_n), \tag{34}$$

$$P = \begin{bmatrix} p_1(\vec{x}_1) & p_2(\vec{x}_1) & \cdots & p_m(\vec{x}_1) \\ p_1(\vec{x}_2) & p_2(\vec{x}_2) & \cdots & p_m(\vec{x}_2) \\ \vdots & \vdots & \ddots & \vdots \\ p_1(\vec{x}_n) & p_2(\vec{x}_n) & \cdots & p_m(\vec{x}_n) \end{bmatrix} \tag{35}$$

and

$$W(\vec{x}) = \begin{bmatrix} w(\vec{x}-\vec{x}_1) & 0 & \cdots & 0 \\ 0 & w(\vec{x}-\vec{x}_2) & \cdots & 0 \\ \vdots & \vdots & \ddots & \vdots \\ 0 & 0 & \cdots & w(\vec{x}-\vec{x}_n) \end{bmatrix}, \tag{36}$$

n is the number of points. The extremum of J is given as

$$\frac{\partial J}{\partial a} = A(\vec{x})a(\vec{x}) - B(\vec{x})\hat{z} = 0, \tag{37}$$

where

$$A(\vec{x}) = P^T W(\vec{x}) P, \tag{38}$$

$$B(\vec{x}) = P^T W(\vec{x}). \tag{39}$$

Then a is given as

$$a(\vec{x}) = A^{-1}(\vec{x})B(\vec{x})\hat{z}, \tag{40}$$

here

$$\hat{z} = [z(\vec{x}_1), z(\vec{x}_2) \cdots z(\vec{x}_n)]^T. \tag{41}$$

The expression for $z^h(\vec{x})$ is written as

$$z^h(\vec{x}) = P(\vec{x})A^{-1}(\vec{x})B(\vec{x})\hat{z} = \Phi^T(\vec{x})\hat{z} \tag{42}$$

in which $\Phi(\vec{x})$ is the shape function as below

$$\Phi^T(\vec{x}) = [\varphi_1, \varphi_2, \ldots, \varphi_n] = P^T(\vec{x})A^{-1}(\vec{x})B(\vec{x}). \tag{43}$$

The first derivative and second derivative of the shape function are respectively given as

$$\Phi^T_{,i} = P^T_{,i}A^{-1}B + P^TA^{-1}_{,i}B + P^TA^{-1}B_{,i}, \tag{44}$$

$$\Phi^T_{,ij} = P^T_{,ij}A^{-1}B + P^T_{,i}A^{-1}_{,j}B + P^T_{,i}A^{-1}B_{,j} + P^T_{,j}A^{-1}_{,i}B + P^TA^{-1}_{,ij}B + P^TA^{-1}_{,i}B_{,j} + P^T_{,j}A^{-1}B_{,i} + P^TA^{-1}_{,j}B_{,i} + P^TA^{-1}B_{,ij}. \tag{45}$$

Then the first derivative and second derivative of the surface function are given in the following:

$$z^h_{,i} = \Phi^T_{,i}\hat{z}, \tag{46}$$

$$z^h_{,ij} = \Phi^T_{,ij}\hat{z}. \tag{47}$$

The derivatives of surface function will be used in the calculation of the normal vector and curvature of the boundary surface.

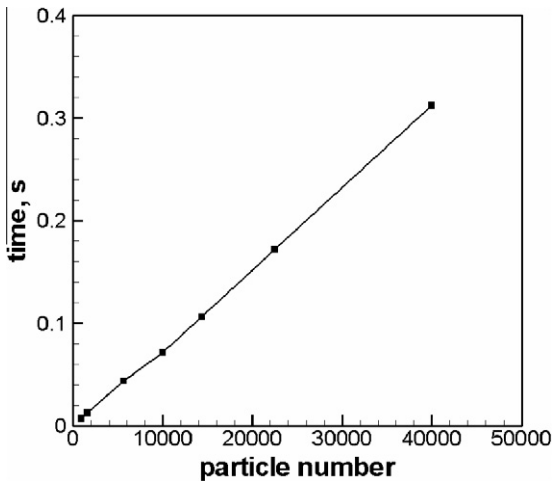

Fig. 3. Run time of the algorithm of 2D surface tension model vs. particle number (2D square).

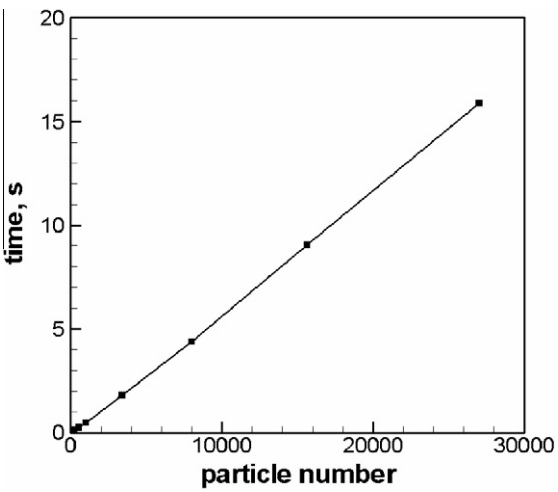

Fig. 4. Run time of the algorithm of 3D surface tension model vs. particle number (3D cube).

As mentioned above, the surface function is obtained by MLS. The surface function can be rewritten as

$$z = f(x,y). \tag{48}$$

The boundary surface can be parametrized as

$$\vec{r}(x,y) = \langle x, y, f(x,y)\rangle. \tag{49}$$

2.2.3. Curvature and the normal vector of the interface in 3D

Based on the parametric surface $\vec{r}(x,y)$, the normal vector and curvature of the boundary surface can be calculated. The unit normal vector is given as

$$\vec{n} = \frac{\vec{r}_x \times \vec{r}_y}{|\vec{r}_x \times \vec{r}_y|} = \langle -f_x, -f_y, 1\rangle \cdot \frac{1}{\sqrt{1+f_x^2+f_y^2}}, \tag{50}$$

where f_x and f_y are the derivative of surface function $f(x,y)$ with respect to x and y, respectively. f_x and f_y can be obtained by Eq. (46).

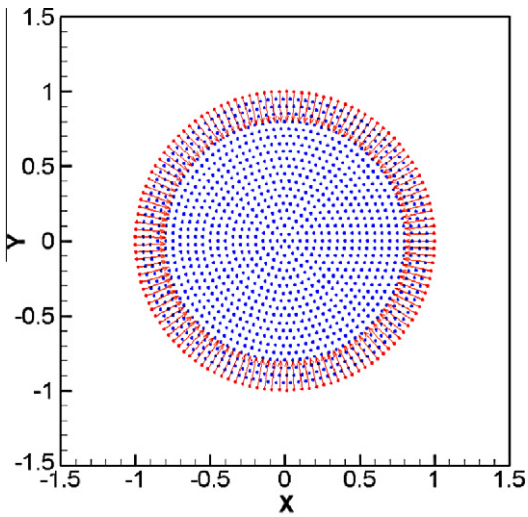

Fig. 5. Particle position of 2D circle with the normal vector on the surface (with 125 boundary particles).

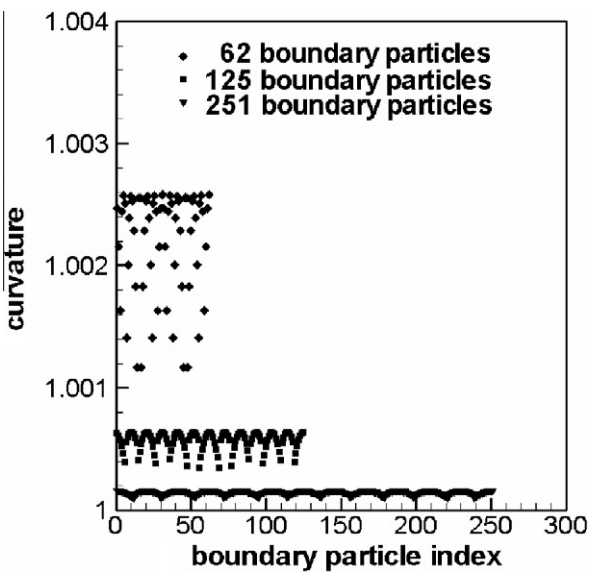

Fig. 6. The curvature of the reconstructed surface of 2D circle with radius of 1.

Before computation of curvature of the boundary surface, the coefficients in the first fundamental form and second fundamental form of the boundary surface should be given. The first fundamental form of boundary surface is a quadratic form

$$I = Edx^2 + 2Fdxdy + Gdy^2. \tag{51}$$

The coefficients can be obtained as follows:

$$E = \vec{r}_x \cdot \vec{r}_x = 1 + f_x^2, \tag{52}$$
$$F = \vec{r}_x \cdot \vec{r}_y = f_x f_y, \tag{53}$$
$$G = \vec{r}_y \cdot \vec{r}_y = 1 + f_y^2. \tag{54}$$

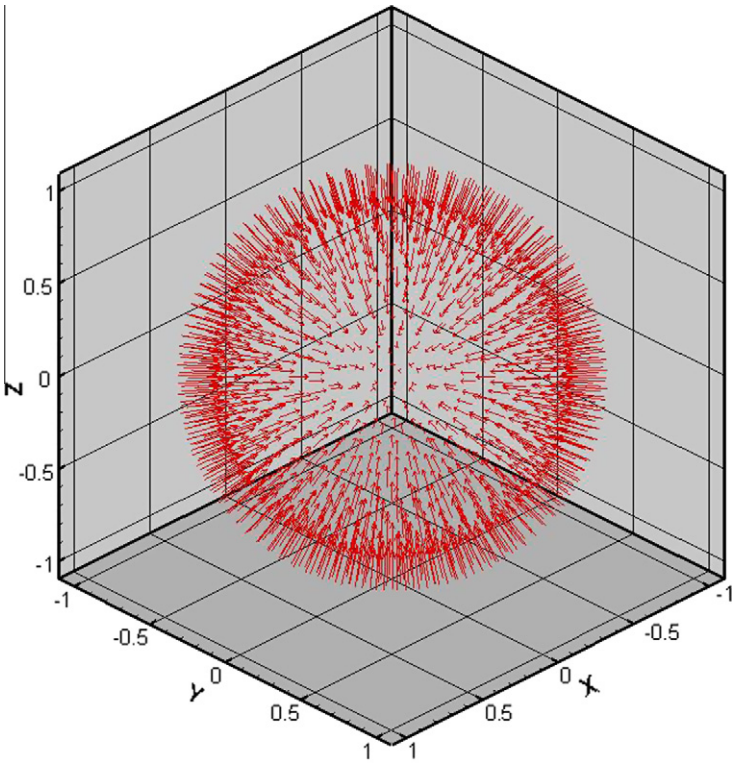

Fig. 7. The normal vector on the surface of 3D sphere (with 1220 boundary particles).

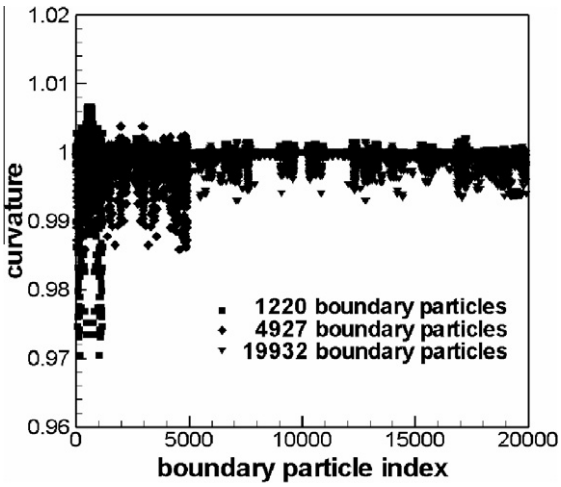

Fig. 8. The curvature of the reconstructed surface of 3D sphere with radius of 1.

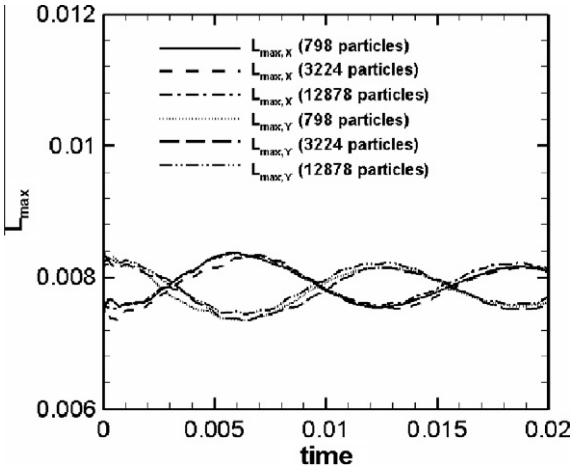

Fig. 9. Maximum extension of a deformed drop along x and y axes.

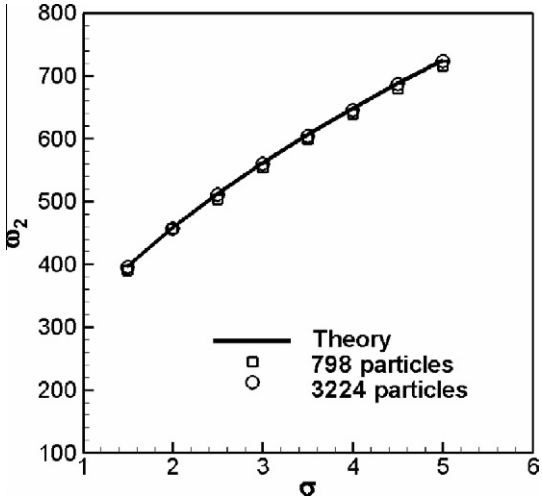

Fig. 10. The frequency of drop with initial aspect ratio 1.1 in 2D vs. the coefficient of surface tension.

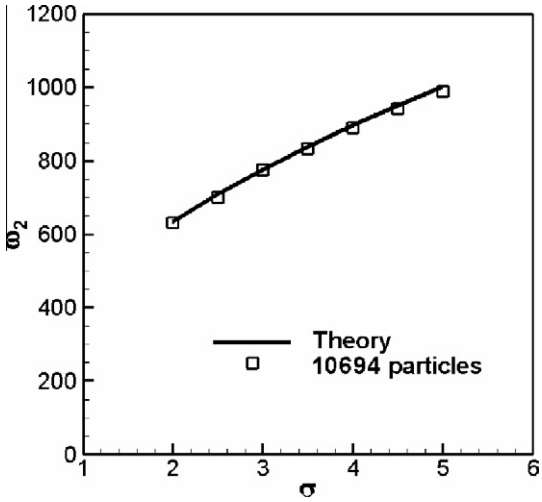

Fig. 11. The frequency of drop with initial aspect ratio 1.1 in 3D vs. the coefficient of surface tension.

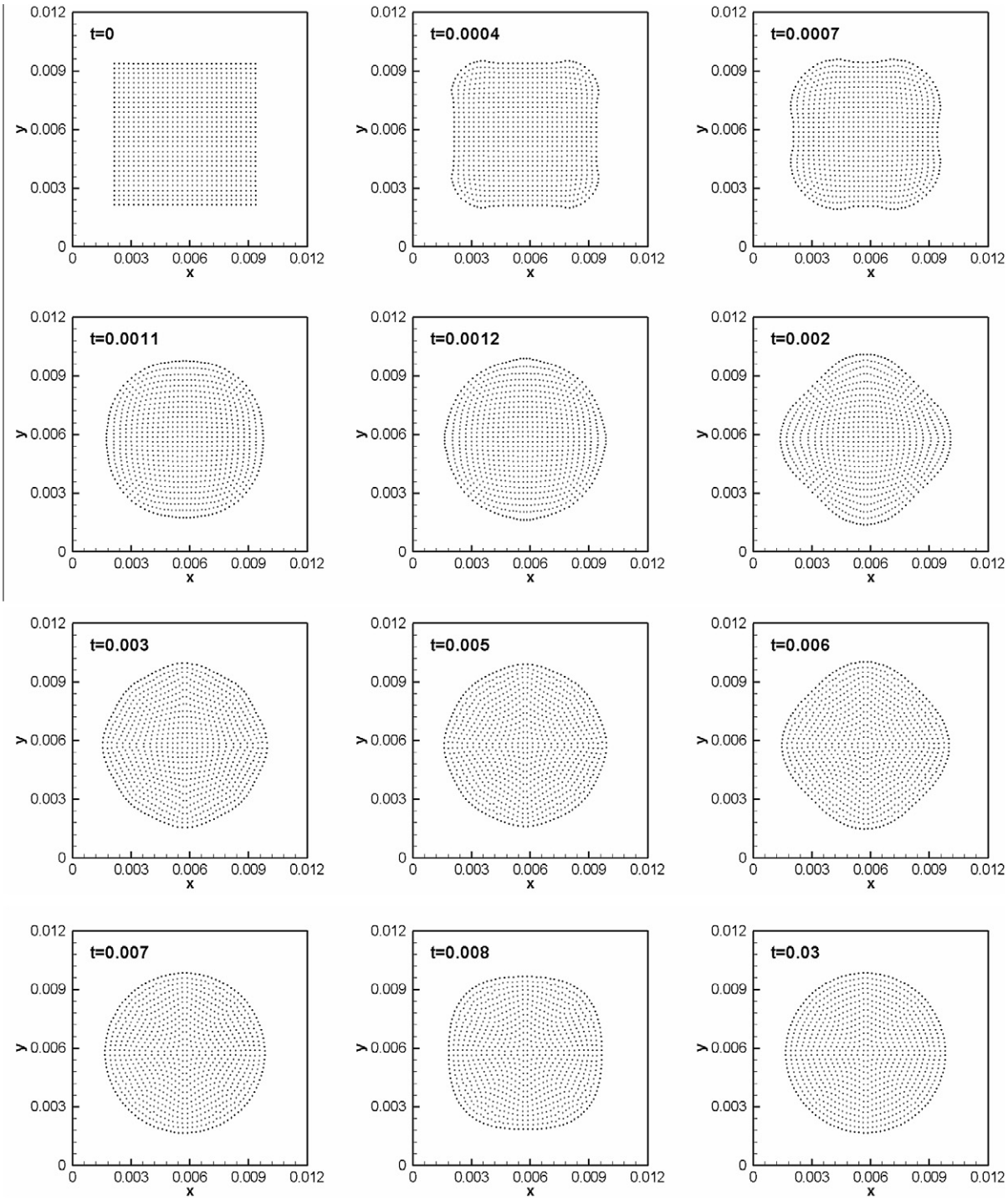

Fig. 12. The snapshot of oscillation of 2D liquid drop with initial shape of square.

The second fundamental form of boundary surface is

$$II = Ldx^2 + 2Mdxdy + Ndy^2. \tag{55}$$

The coefficients can be calculated as below

$$L = \vec{r}_{xx} \cdot \vec{n} = \frac{f_{xx}}{\sqrt{1+f_x^2+f_y^2}}, \tag{56}$$

$$M = \vec{r}_{xy} \cdot \vec{n} = \frac{f_{xy}}{\sqrt{1+f_x^2+f_y^2}}, \tag{57}$$

$$N = \vec{r}_{yy} \cdot \vec{n} = \frac{f_{yy}}{\sqrt{1+f_x^2+f_y^2}}. \tag{58}$$

Then the mean curvature of boundary surface can be given as

$$H = \frac{1}{2} \cdot (\kappa_1 + \kappa_2) = \frac{EN - 2FM + GL}{2(EG - F^2)} = \frac{(1+f_x^2)f_{yy} - 2f_x f_y f_{xy} + (1+f_y^2)f_{xx}}{2(1+f_x^2+f_y^2)^{3/2}},$$

where f_{xx}, f_{xy}, f_{yy} are the second derivative of surface function $f(x,y)$ and can be calculated by Eq. (47).

The unit normal vector and curvature can be obtained by Eqs. (50) and (59), respectively. Then surface tension force can be calculated by Eq. (7).

3. Results and discussion

To approve the ability of the current method in the simulation of free surface problem in vacuum, numerical examples in 2D and 3D are given in the following. The current method is robust and efficient to handle the interfacial problem with surface tension in vacuum. To make sure that the SPH particles have homogeneous distribution, XSPH is used in the simulation [24]. The summation density is normalized on the boundary. If not specified otherwise, the parameters used in the calculation in both 2D and 3D are taken as follows. The SPH particles of equal mass have the uniform initial inter-particle distance of

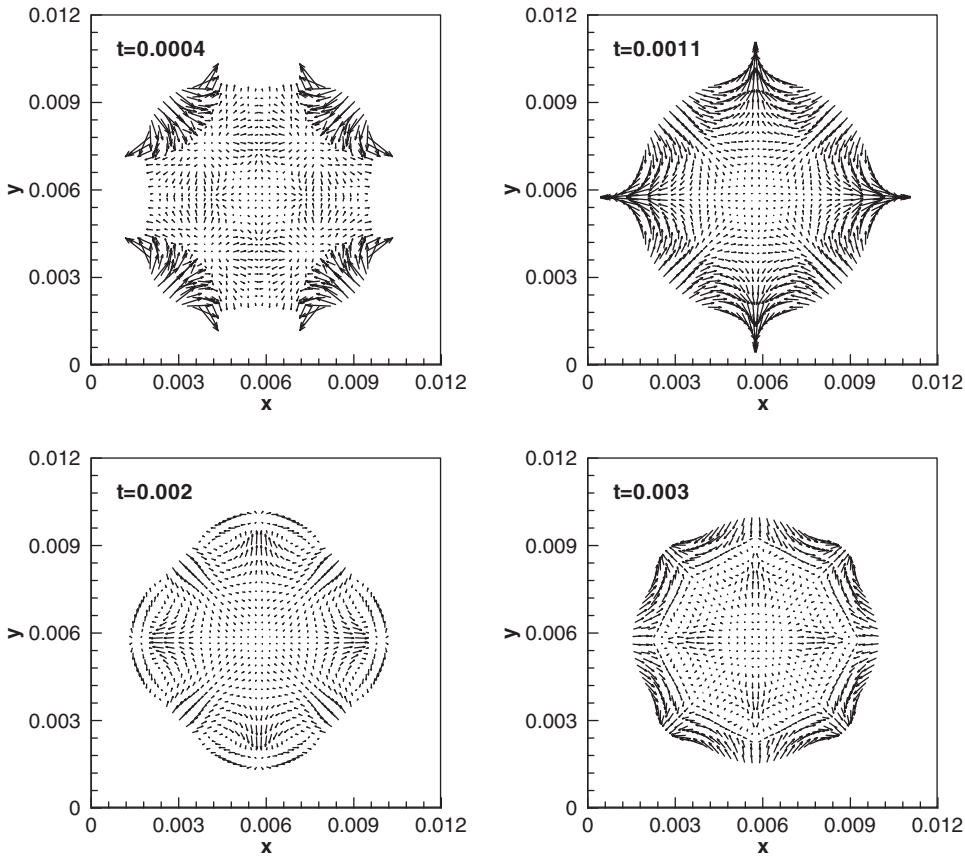

Fig. 13. Velocity field for oscillation of 2D liquid drop with initial shape of square.

0.25×10^{-3}. The constant smoothing length is equal to the initial inter-particle distance. The reference density is taken as 1000. The cubic spline kernel is used as the smoothing function in the calculation. The predictor–corrector scheme is used in the time integration. And the time step is controlled by CFL condition $\left(\Delta t \leqslant 0.25\frac{h}{c}\right)$, the viscous-diffusion condition $\left(\Delta t \leqslant 0.25\frac{h^2}{\nu}\right)$ and surface tension condition $\left(\Delta t \leqslant 0.25\left(\frac{\rho h^3}{2\pi\sigma}\right)^{1/2}\right)$ [19].

3.1. Efficiency and accuracy

As stated in Refs. [21,22], the complexity of the algorithms for the boundary particle detection in 2D and in 3D are $NN_a \log N_a$ and NN_a^2, respectively, where N is the total number of particles and N_a is the average number of the neighbors per particle. The computation for the reconstruction of interface is also linear with the total number of particles. 2D square test and 3D cube test are used in 2D and 3D, respectively. During the tests, the number of neighbors per particle is approximate the same and the total number of particles increase. Figs. 3 and 4 prove that the run time of the current algorithms for surface tension is linear with the total number of particles in both 2D and 3D. The current algorithm has higher efficiency.

The accurate computations of normal vector and curvature of the interface are the most important issues in the computation of surface tension force. To validate the current method for surface tension, the computations of normal vector and curvature of the interface on circle and sphere are studied. Fig. 5 gives the calculated normal vector on the surface of the circle. Fig. 6 gives the curvature of the circle with radius of 1. In theory, the curvature of the circle is inverse of the radius of the circle. Fig. 6 shows that the calculated curvature converges to 1 by increasing the number of the boundary particles. The maximum relative error for the 62, 125, and 251 boundary particles are 2.6×10^{-3}, 6.3×10^{-4}, and 1.6×10^{-4}, respectively. Fig. 7 gives the normal vector on the surface of the sphere. Fig. 8 gives the curvature of the sphere with radius of 1. The curvature of sphere is the inverse of the radius of the sphere. Fig. 8 shows that the calculated curvature converges to theoretic value 1 by increasing the number of the boundary particles. The maximum relative error for the 1220, 4927, and 19,932 boundary particles are 0.0296, 0.0142, and 0.00697, respectively. The accurate normal vector and curvature can be obtained by the current method.

To further validate the current method, the oscillations of drop are numerically investigated. The density of the drop is 1000 and the viscosity is set to 0.001. The initial aspect ratio of the deformed drop is 1.1. Fig. 9 shows the maximum extension of a deformed drop along x and y axes. The coefficient of surface tension is 2.5. 798, 3224, and 12,878 particles are used in the simulation. In the classical work by Rayleigh [27], the normal-mode frequencies for an oscillating drop are given by

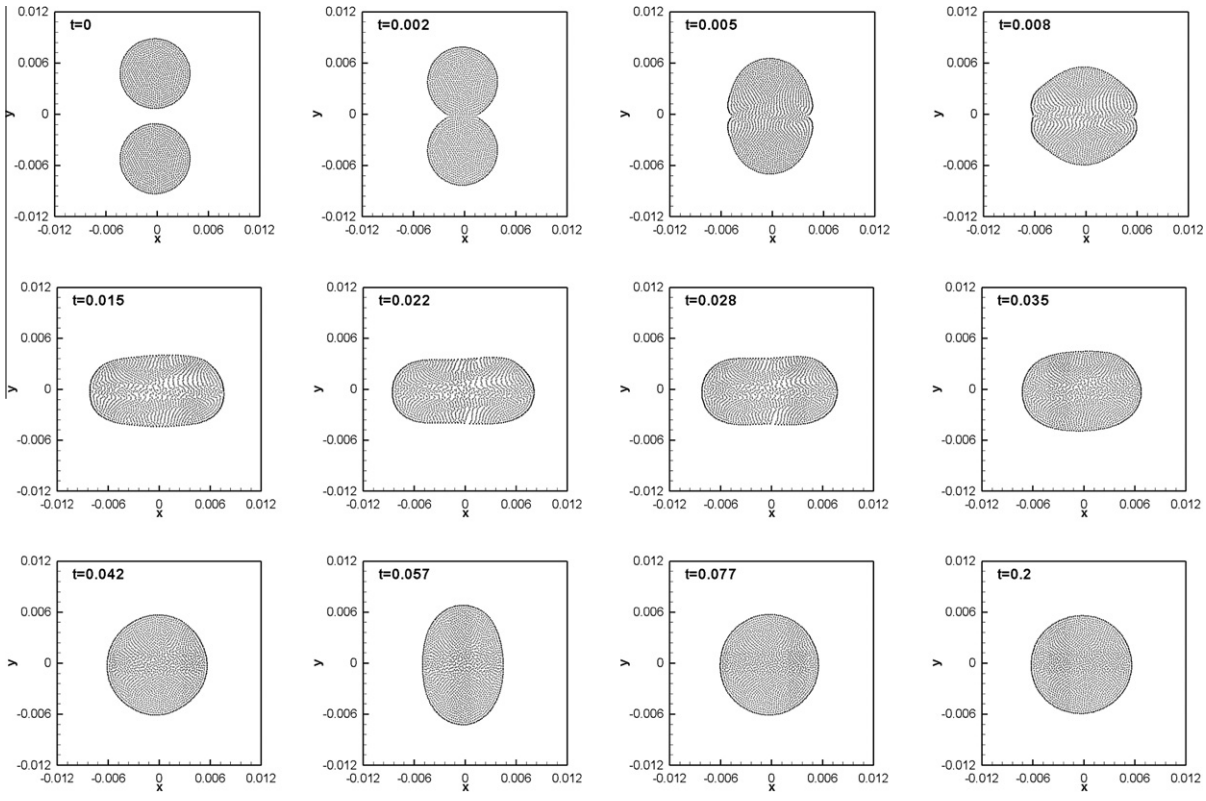

Fig. 14. 2D head-on binary collision with the relative velocity 1.0. The time is shown in each panel.

$$\omega_n^2 = n(n-1)(n+2)\frac{\sigma}{\rho R^3},$$

where $n = 2,3,\ldots$, stands for the mode number. The normal-mode frequencies for 2D oscillating drops are [27]

$$\omega_n^2 = n(n^2-1)\frac{\sigma}{\rho R^3}. \tag{61}$$

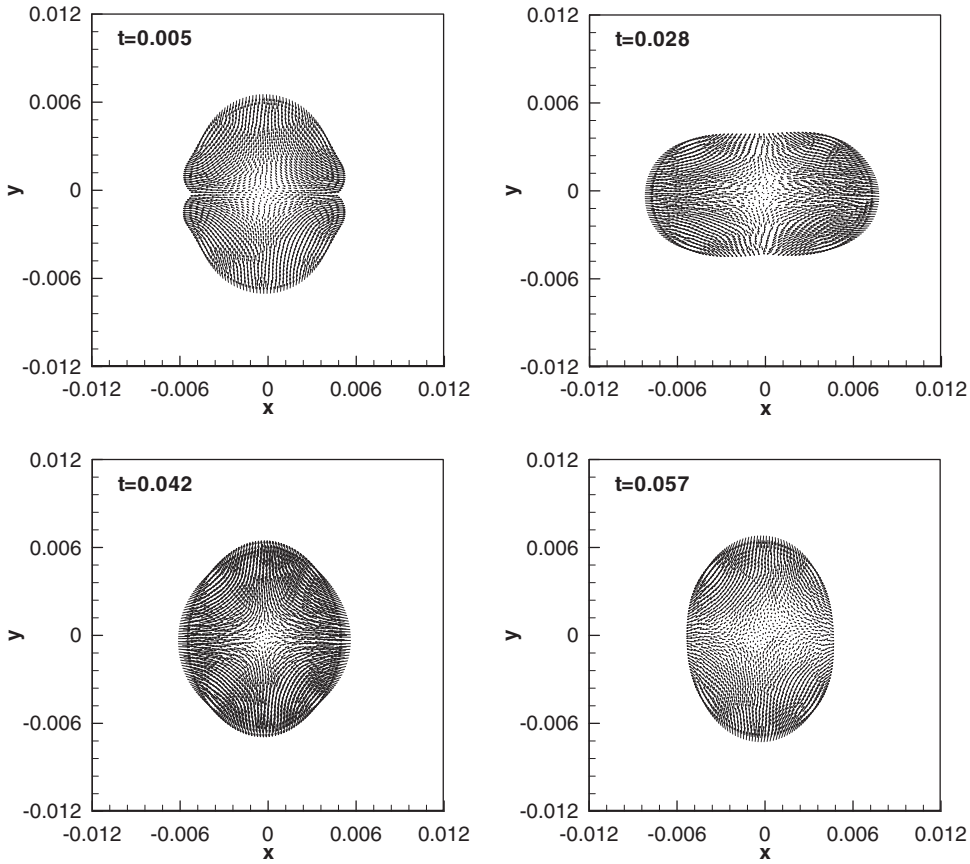

Fig. 15. Velocity field at $t = 0.005$, 0.028, 0.042, and 0.057 for the 2D head-on binary collision with relatively velocity 1.0. The maximum velocity is 0.398, 0.108, 0.163, and 0.0136 at $t = 0.005$, 0.028, 0.042, and 0.057, respectively.

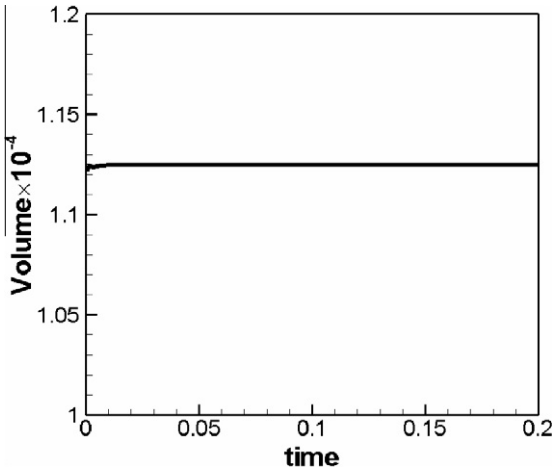

Fig. 16. The volume of the coalesced drop vs. time during the 2D head-on binary collision.

Fig. 10 shows that the frequency of drop with initial aspect ratio 1.1 in 2D as a function of the coefficient of surface tension. According to the Eq. (61) with $n = 2$, the theoretical value for the normal-mode frequency in 2D is $\sqrt{\frac{6\sigma}{\rho R^3}}$. The maximum relative errors for 798 and 3224 particles are 0.021 and 0.0043, respectively. The numerical results demonstrate convergence of the current method. Fig. 11 shows that the frequency of drop with initial aspect ratio 1.1 in 3D as a function of the coefficient of surface tension. From the Eq. (60) with $n = 2$, the theoretical value for the normal-mode frequency in 3D is $\sqrt{\frac{8\sigma}{\rho R^3}}$. Ten thousand six hundred and ninety four particles are used in the simulation. The maximum relative error is 0.011. The numerical results in both 2D and 3D agree well with theory.

3.2. Numerical examples in 2D

3.2.1. Oscillation of 2D square liquid drop

Deformation of 2D liquid drop from initial shape of square to a circle is simulated. The side length of the square is 7.5×10^{-3} and 900 SPH particles are used in the simulation. The coefficient of surface tension is set to 2.5. The viscosity of the liquid is 1.0×10^{-6}.

Fig. 12 shows the snapshots of oscillation of 2D liquid drop with initial shape of square in sequence. Fig. 13 shows the velocity field of oscillation of 2D liquid drop. Due to surface tension force on the interface, the SPH particles at the corner

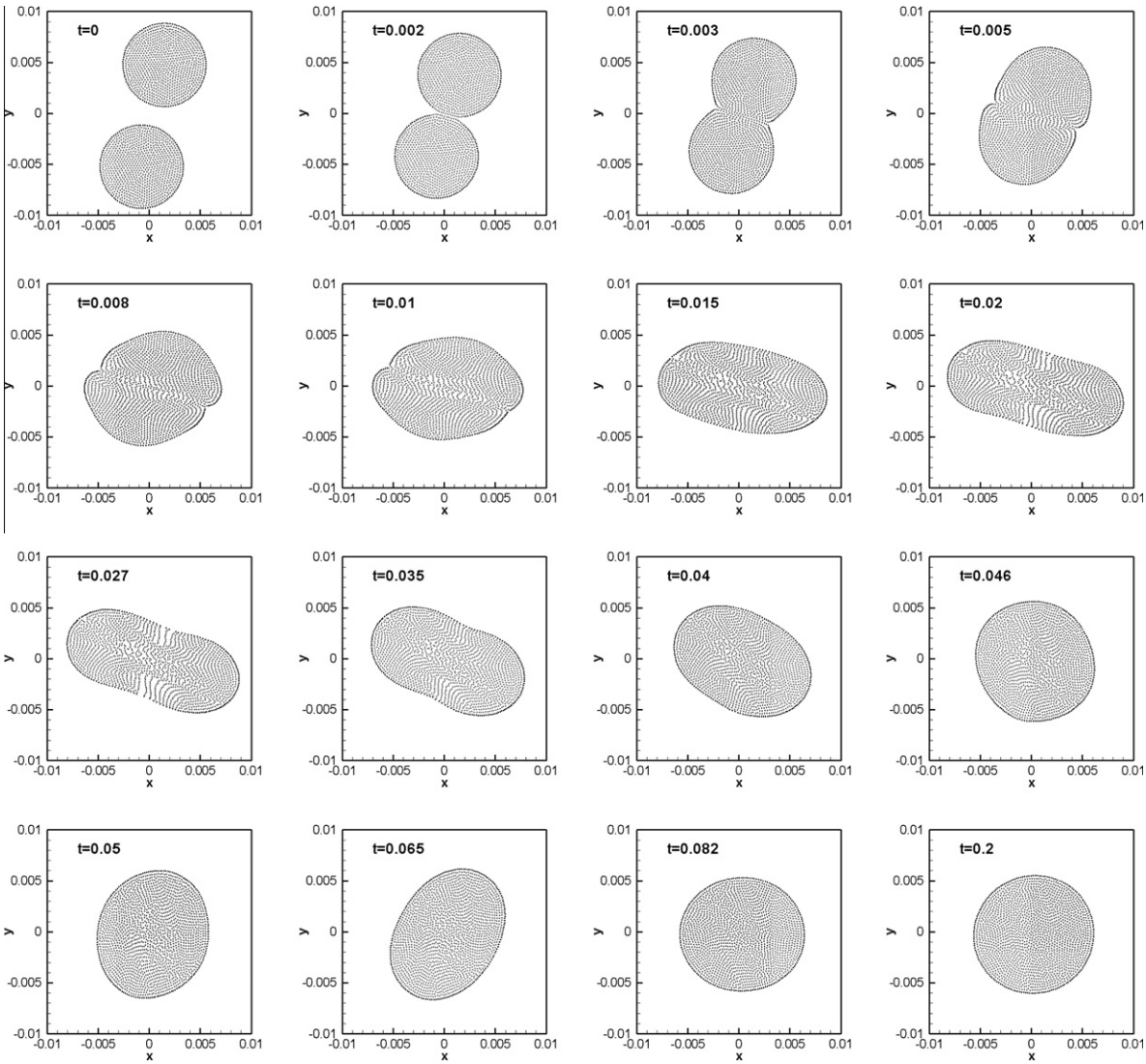

Fig. 17. 2D off-center binary collision with the relative velocity 1.0. The time is shown in each panel.

have velocities towards the center of the liquid square at the beginning. Since surface tension force is proportional to the curvature of the interface, the velocities are larger around the corners as shown at $t = 0.0004$ in Fig. 13. At $t = 0.0011$, the shape of 2D liquid drop is similar to a circle. However, 2D liquid drop is not at equilibrium. The SPH particles at the interface near the x axis and y axis have large velocities with outward direction. It results in the shape of the diamond at $t = 0.0012$. During the oscillation of 2D liquid drop, the kinetic energy dissipates due to the liquid viscosity. The 2D liquid drop evolves into the flower, non-equilibrium circle, diamond, round-corner square, final circle in equilibrium.

3.2.2. 2D head-on binary collision

2D head-on collision of two drops with equal size is simulated by using the current method. The relative velocity of two drops is 1.0. The total number of SPH particles in the simulation is 1800. The coefficient of surface tension is set to 0.25. The viscosity of the liquid is 0.1. The Reynolds number is 83 and the Weber number is 33.2.

Fig. 14 shows the evolution of head-on binary collision with the relative velocity 1.0 in the first period. As two drops touch with each other, the liquid bridge forms between two drops. And the liquid bridge grows with time during the coalescence of the two drop. The elongation along the x axis results from the high stagnation pressure in the enter region of the coalesced drop. After the coalesced drop reaches its maximum deformation at $t = 0.0022$, the kinetic energy completely converts into surface energy and the coalesced drop begins to contract along the x axis. And the shape of 'peanut' is formed at $t = 0.0028$. The coalesced drop evolves into the non-equilibrium circle at $t = 0.0042$. The coalesced drop completes its first period of oscillation at $t = 0.057$ and the aspect ratio is 1.5 (less than its largest aspect ratio 2.33 at t 0.0022) at that time.

Fig. 15 shows the velocity field of 2D head-on binary collision at $t = 0.005$, 0.028, 0.042, and 0.057. As two drops touch with each other, the velocity of the drop in the y direction reduces and the stagnation pressure at the center of the coalesced drop increases. The high stagnation pressure results in the side movement of the coalesced drop along the x axis. The stagnation flow forms at the center of the coalesced drop as shown in Fig. 15 because of the internal counter-flow in the coalesced drop. As there is no external force, the velocity field in the coalesced drop is symmetric. Fig. 16 shows that the total volume of the coalesced drop keeps approximately constant.

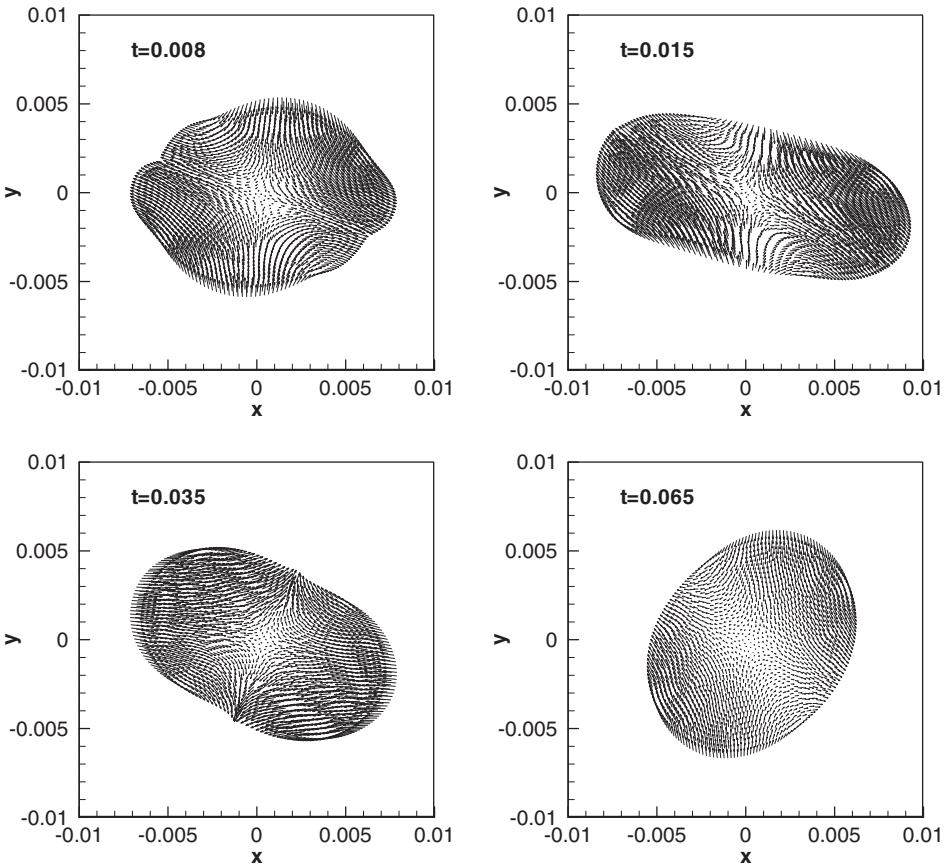

Fig. 18. Velocity field at $t = 0.008$, 0.015, 0.035, and 0.065 for the 2D off-center binary collision with relatively velocity 1.0. The maximum velocity is 0.436, 0.213, 0.167, and 0.0576 at $t = 0.008$, 0.015, 0.035, and 0.065, respectively.

3.2.3. 2D off-center binary collision

2D off-center collision of two drops with equal size is simulated by using the current method. The relative velocity of two drops is 1.0 and the impact parameter χ ($=\frac{X}{D}$, X is the perpendicular component of the distance between two drops center relative to the impact velocity, D is the drop diameter) is 0.5. The total number of SPH particles in the simulation is 1800. The coefficient of surface tension is set to 0.25. The viscosity of the liquid is 0.1. The Reynolds number is 83 and the Weber number is 33.2.

Fig. 17 shows the evolution of 2D off-center binary collision. Similar with the evolution of head-on binary collision, the liquid bridge forms at the contact point as two drops touch with each other. The liquid bridge grows with the mergence of two drops. The stagnation pressure increases and results in the elongation of coalesced drop. The coalesced drop evolves into the shapes of 'peanut', non-equilibrium circle, and final circle in equilibrium. One different feature of off-center collision from head-on collision is that the point symmetric shape of the coalesced drop induces the rotational motion. It is similar with the results from Melean and Sigalotti [12].

Fig. 18 shows the velocity field of 2D off-center binary collision at t = 0.008, 0.015, 0.035, and 0.065. The stagnation flow is formed at the center of the coalesced drop as shown in Fig. 18. It results from the point symmetry motion. As shown at

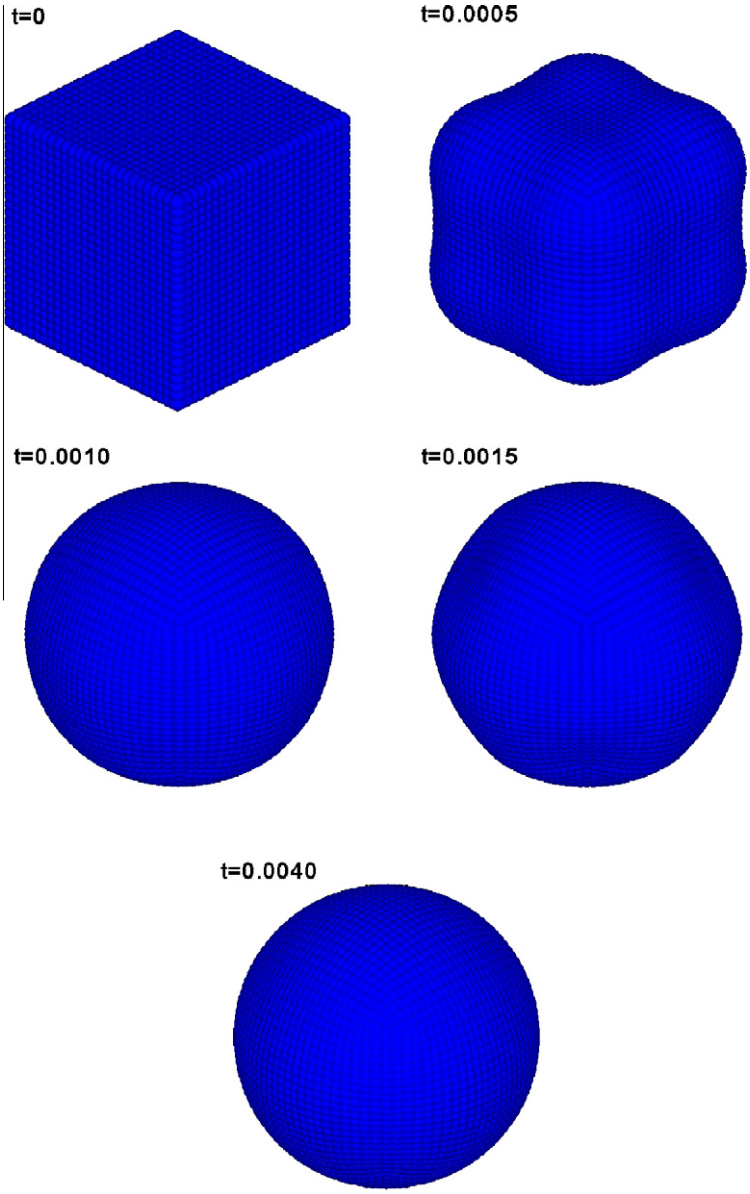

Fig. 19. The snapshot of oscillation of cubic liquid drop.

$t = 0.035$ in Fig. 18, the velocity field is point symmetry and the direction of the velocity is in the clockwise direction relative to the center of coalesced drop. The clockwise distribution of velocity field induces the rotation of the drop.

3.3. Numerical examples in 3D

3.3.1. Oscillation of cubic liquid drop

Deformation of cubic liquid drop to a sphere is simulated. The side length of the cube is 6.25×10^{-3} and 15,625 ($=25^3$) SPH particles are used in the simulation. The coefficient of surface tension is set to 2.5. The viscosity of the liquid is 1.0×10^{-6}.

Fig. 19 shows the snapshot of oscillation of cubic liquid drop. Fig. 20 shows the magnitude of velocity at $t = 0.0005$, 0.001, 0.0015, and 0.004 for oscillation of cubic liquid drop. Due to surface tension force on the surface of cubic liquid drop, the eight corners of cubic liquid drop deform first. The liquid drop evolves into dumbbell shape and has larger velocity at the corners at $t = 0.0005$ as shown in Figs. 19 and 20. The eight round corners of liquid drop continue to contract and have a shape of non-equilibrium sphere at $t = 0.001$ as shown in Figs. 19 and 20. The liquid drop becomes a drop with a shape of the diamond at $t = 0.0015$. Due to the viscous dissipation, the liquid drop evolves into a sphere at equilibrium at $t = 0.004$. During the oscillation, cubic liquid drop evolves into dumbbell, non-equilibrium sphere, diamond, sphere at equilibrium.

3.3.2. 3D head-on binary collision

3D head-on collision of two drops with equal size is simulated by using the current method. The relative velocity of two drops is 1.0. The total number of SPH particles in the simulation is 16,000 ($=2 \times 20^3$). The coefficient of surface tension is set to 2.5. The viscosity of the liquid is 0.1. The Reynolds number is 74 and the Weber number is 2.96.

Fig. 21 shows head-on binary collision with the relative velocity 1.0. Fig. 22 shows magnitude of velocity for head-on binary collision with the relative velocity 1.0. As two liquid drops touch with each other, the liquid bridge forms between two drops. The radius of liquid bridge increases as two drops coalesce. The kinetic energy of drop converts into the kinetic energy

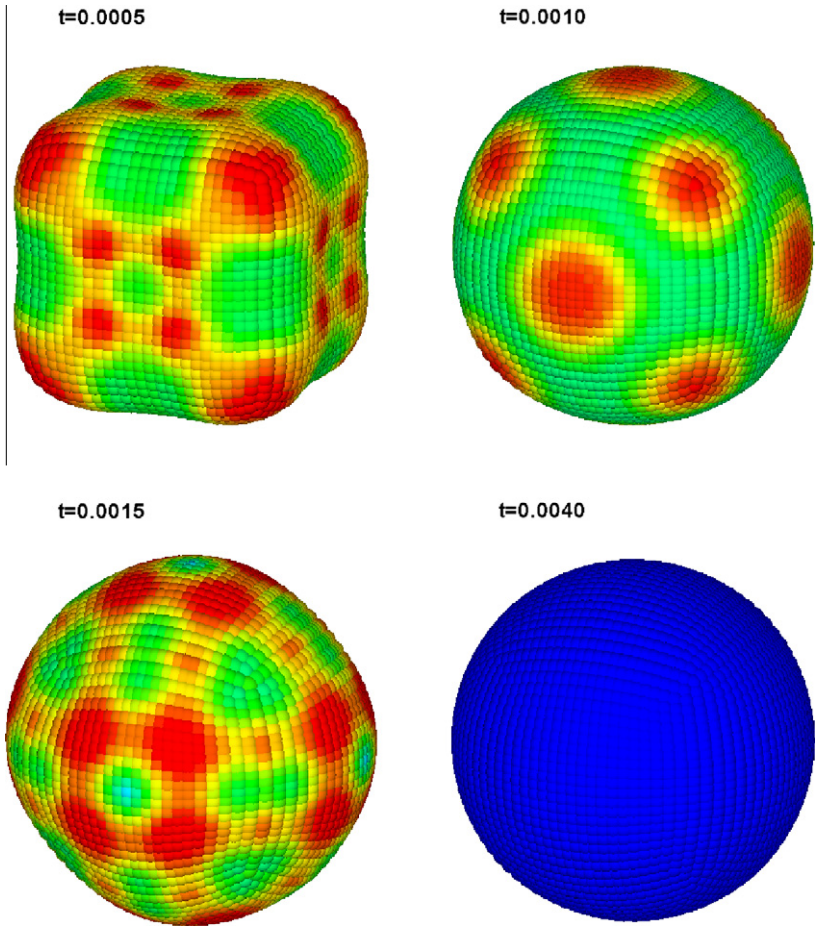

Fig. 20. Magnitude of velocity at $t = 0.0005$, 0.001, 0.0015, and 0.004 for oscillation of cubic liquid drop. The maximum velocity is 1.22, 1.09, 0.71 and 0.054 at $t = 0.0005$, 0.001, 0.0015, and 0.004, respectively.

of the liquid bridge. The stagnation region forms in the liquid bridge and high stagnation pressure results in the deformation of the coalesced drop in the horizontal direction. The velocity of the drop in the horizontal direction increases with the formation of the liquid bridge. The coalesced drop elongates along the horizontal direction and reaches its maximum deformation at $t = 0.0058$ as shown in Figs. 21 and 22. Then the contraction of the coalesced drop in the horizontal direction is followed. The non-equilibrium sphere is formed at $t = 0.0077$ as shown in Figs. 21 and 22. The coalesced drop continues to deform and elongate and contraction is followed at $t = 0.0105$ and 0.0128. Finally, the sphere at equilibrium is formed at $t = 0.016$.

3.3.3. 3D off-center binary collision

3D off-center of two drops with equal size is simulated by using the current method. The relative velocity of two drops is 1.0 and the impact parameter χ ($=\frac{X}{D}$, X is the perpendicular component of the distance between two drops center relative to the impact velocity, D is the drop diameter) is 0.5. The total number of SPH particles in the simulation is 16,000 ($=2 \times 20^3$). The coefficient of surface tension is set to 2.5. The viscosity of liquid is 0.1. The Reynolds number is 74 and the Weber number is 2.96.

Fig. 23 shows off-center binary collision with the relative velocity 1.0. As two liquid drops touch with each other, the liquid bridge forms between two drops. The stagnation pressure increases with time and results in the elongation of the coalesced drop. The peanut-shaped drop forms at $t = 0.003$. Similar with the 2D off-center binary collision, the coalesced drop deforms and rotates. Due to the viscous dissipation, the coalesced drop evolves into a sphere at equilibrium.

Fig. 24 shows the magnitude of velocity for off-center binary collision with the relative velocity 1.0. The stagnation flow forms in the center of coalesced drop and the internal motion in the drop is point symmetry. And the direction of the velocity is in the clockwise direction relative to the center of the coalesced drop, as shown in Fig. 24. The clockwise distribution of velocity field induces the rotation of the drop.

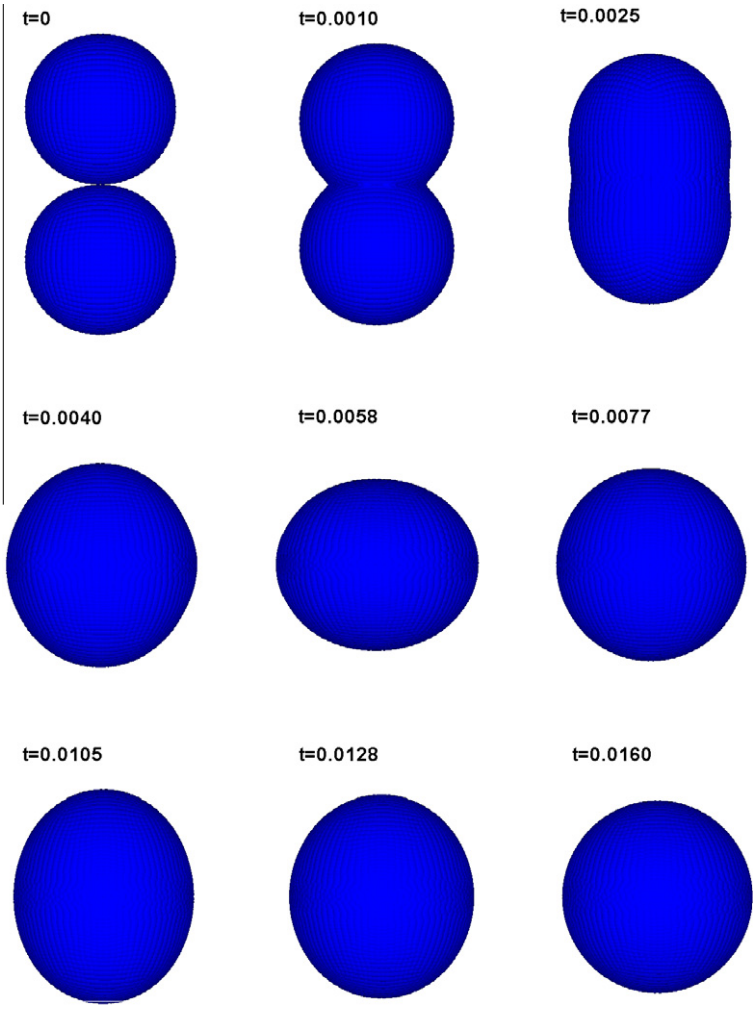

Fig. 21. 3D head-on binary collision with the relative velocity 1.0 (Re = 74, We = 2.96).

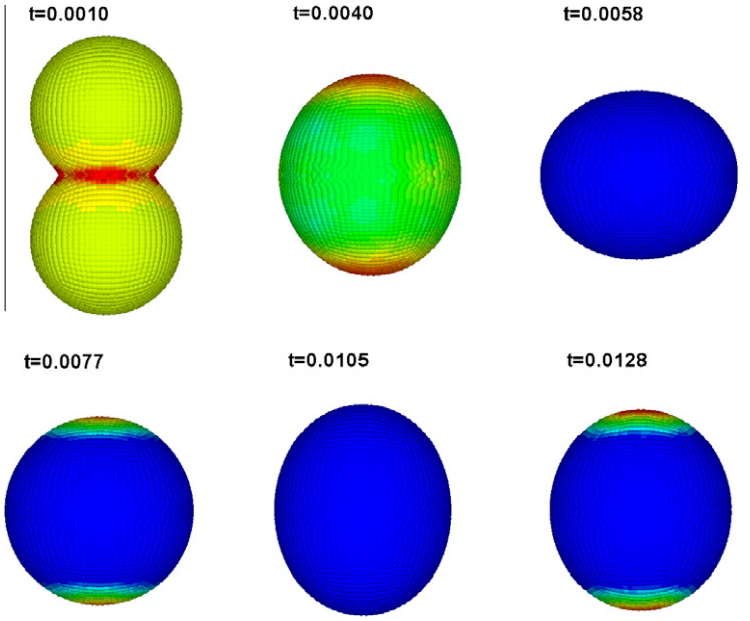

Fig. 22. Magnitude of velocity at $t = 0.001$, 0.004, 0.0058, 0.0077, 0.0105 and 0.0128 for 3D head-on binary collision with the relative velocity 1.0. The maximum velocity is 1.67, 0.63, 0.16, 0.32, 0.058 and 0.14 at $t = 0.001$, 0.004, 0.0058, 0.0077, 0.0105 and 0.0128, respectively.

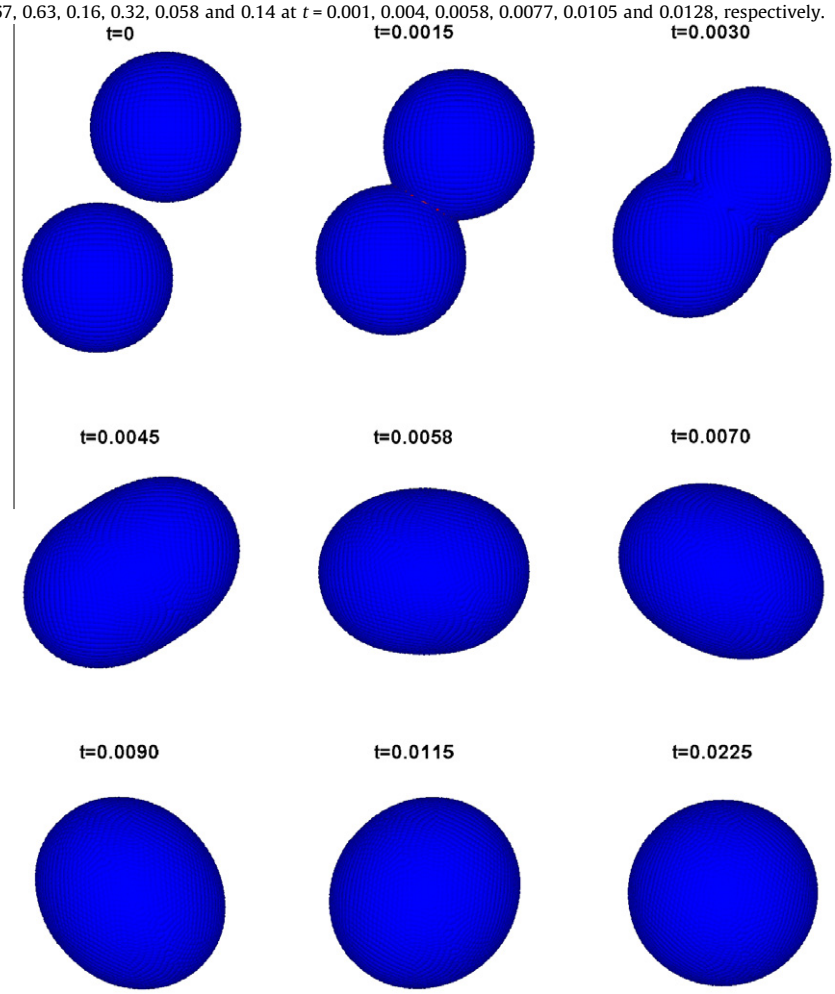

Fig. 23. 3D off-center binary collision with the relative velocity 1.0 (Re = 74, We = 2.96).

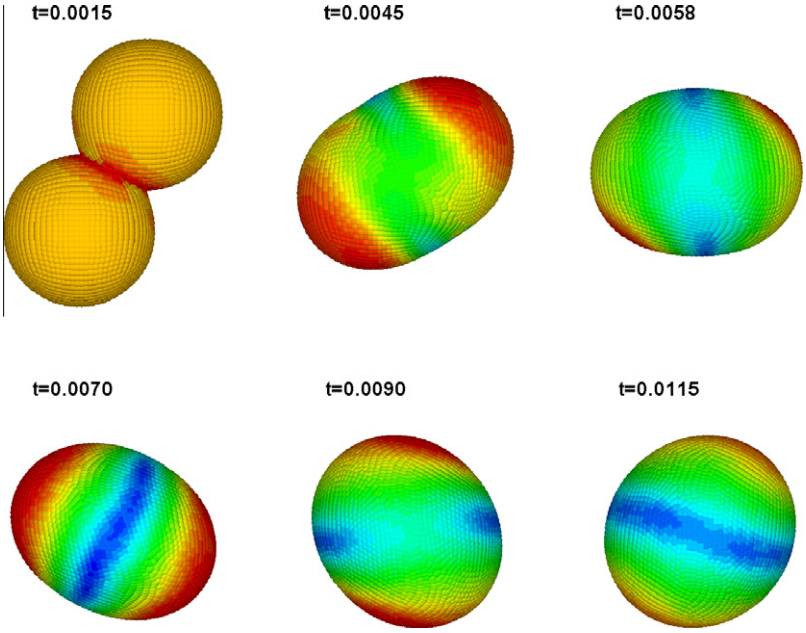

Fig. 24. Magnitude of velocity at $t = 0.0015$, 0.0045, 0.0058, 0.007, 0.009 and 0.0115 for 3D off-center binary collision with the relative velocity 1.0. The maximum velocity is 1.0, 0.65, 0.64, 0.34, 0.35 and 0.19 at $t = 0.0015$, 0.0045, 0.0058, 0.007, 0.009 and 0.0115, respectively.

4. Conclusion

The current method has been applied to simulate free surface problem in vacuum. After detecting the boundary particles, the interfacial is fitted locally by using Lagrangian interpolation polynomial in 2D and by using MSL in 3D, respectively. By transforming the coordinate system, it is guaranteed that the reconstructed interface is one-valued in the local coordinate system. Then surface tension force can be calculated by Eq. (7). In order to reduce the effects of the particle deficiency on the boundary, the density is normalized on the boundary. XSPH is used to make the particle move in order. Based on the developed method, benchmark tests are investigated numerically.

The current method works well in the benchmark tests. The 2D square liquid evolves into the flower, non-equilibrium circle, diamond, round-corner square, final circle in equilibrium. The cubic liquid drop evolves into dumbbell, non-equilibrium sphere, diamond, sphere at equilibrium. The kinetic energy and surface energy convert into each other and the stagnation flow forms during the binary collision. The coalesced drop rotates during the oscillation of the off-center binary collision.

Since the boundary is detected explicitly, surface tension force can be calculated directly on the boundary. It is physically correct that surface tension force acts only on the boundary particle in the current model, since the surface tension force acts on the sharp interface. Surface tension force is given explicitly in the current model. The current model has no relation with the initial temperature and can be applied to the free surface problem with heat transfer. The numerical simulation shows that the current method is successful to apply to the free surface problem in vacuum with low Reynolds number and low Weber number. The stability of the current method has to be improved for higher Reynolds number and higher Weber number. In the current method, surface tension force is acted on the surface particle and works as a discontinuity on the surface. It results in the instability in the numerical simulation. The smoothed version of the current method will be developed in the future. And the current method will be applied to free surface problem with air.

Acknowledgments

The author is grateful for the constructive comments from the reviewers. The author also acknowledges the support from National Natural Science Foundation of China (Grant Nos. 10742002 and 10802011), Scientific Research Foundation for Returned Scholars, Ministry of Education of China, Science Foundation of CAEP (Grant Nos. 2008A0201009 and 2010B0201029), and Joint Fund of NSAF (Grant No. 10676120).

References

[1] L.D. Landau, E.M. Lifshitz, Statistical Physics, Part 1, third ed., Butterworth-Heinemann, 1980.
[2] J.U. Brackbill, D.B. Kothe, C. Zemach, A continuum method for modeling surface tension, Journal of Computational Physics 100 (2) (1992) 335–354.

[3] M. Sussman, P. Smereka, S. Osher, A level set approach for computing solutions to incompressible two-phase flow, Journal of Computational Physics 114 (1) (1994) 146–159.
[4] Y.C. Chang, T.Y. Hou, B. Merriman, S. Osher, A level set formulation of Eulerian interface capturing methods for incompressible fluid flows, Journal of Computational Physics 124 (1996) 449–464.
[5] M. Bussmann, J. Mostaghimi, S. Chandra, On a three-dimensional volume tracking model of droplet impact, Physics of Fluids 11 (6) (1999).
[6] M. Bussmann, S. Chandra, J. Mostaghimi, Modeling the splash of a droplet impacting a solid surface, Physics of Fluids 12 (12) (2000).
[7] M.Y. Zhang, H. Zhang, L.L. Zheng, Application of smoothed particle hydrodynamics method on free surface and solidification problems, Numerical Heat Transfer, Part A: Applications 52 (4) (2007) 299–314.
[8] M.Y. Zhang, H. Zhang, L.L. Zheng, Simulation of droplet spreading, splashing and solidification using smoothed particle hydrodynamics method, International Journal of Heat and Mass Transfer 51 (2008) 3410–3419.
[9] M.Y. Zhang, H. Zhang, L.L. Zheng, Numerical investigation of substrate melting and deformation during thermal spray coating by SPH method, Plasma Chemistry and Plasma Processing 29 (2009) 55–68.
[10] S. Nugent, H.A. Posch, Liquid drops and surface tension with smoothed particle applied mechanics, Physical Review E 62 (4) (2000) 4968–4975.
[11] Y. Melean, L.D.G. Sigalotti, A. Hasmy, On the SPH tensile instability in forming viscous liquid drops, Computer Physics Communications 157 (3) (2004) 191–200.
[12] Y. Melean, L.D.G. Sigalotti, Coalescence of colliding van der Waals liquid drops, International Journal of Heat and Mass Transfer 48 (19–20) (2005) 4041–4061.
[13] H. López, L.D.G. Sigalotti, Oscillation of viscous drops with smoothed particle hydrodynamics, Physical Review E 73 (2006) 12.
[14] A. Colagrossi, M. Landrini, Numerical simulation of interfacial flows by smoothed particle hydrodynamics, Journal of Computational Physics 191 (2003) 448–475.
[15] A.M. Tartakovsky, P. Meakin, Modeling of surface tension and contact angles with smoothed particle hydrodynamics, Physical Review E – Statistical, Nonlinear, and Soft Matter Physics 72 (2) (2005) 1–9.
[16] A.M. Tartakovsky, P. Meakin, A smoothed particle hydrodynamics model for miscible flow in three-dimensional fractures and the two-dimensional Rayleigh–Taylor instability, Journal of Computational Physics 207 (2005) 610–624.
[17] J.P. Morris, Simulating surface tension with smoothed particle hydrodynamics, International Journal for Numerical Methods in Fluids 33 (3) (2000) 333–353.
[18] X.Y. Hu, N.A. Adams, A multi-phase SPH method for macroscopic and mesoscopic flows, Journal of Computational Physics 213 (2) (2006) 844–861.
[19] X.Y. Hu, N.A. Adams, An incompressible multi-phase SPH method, Journal of Computational Physics 227 (1) (2007) 264–278.
[20] X.Y. Hu, N.A. Adams, A constant-density approach for incompressible multi-phase SPH, Journal of Computational Physics 228 (2009) 2082–2091.
[21] G.A. Dilts, Moving least-squares particle hydrodynamics II: conservation and boundaries, International Journal for Numerical Methods in Engineering 48 (2000) 1503–1524.
[22] A. Haque, G.A. Dilts, Three-dimensional boundary detection for particle methods, Journal of Computational Physics 226 (2007) 1710–1730.
[23] P.W. Randles, L.D. Libersky, Smoothed particle hydrodynamics: some recent improvements and applications, Computer Methods in Applied Mechanics and Engineering 139 (1–4) (1996) 375–408.
[24] J.J. Monaghan, Smoothed particle hydrodynamics, Annual Review of Astronomy and Astrophysics 30 (1992) 32.
[25] G.R. Liu, M.B. Liu, Smoothed Particle Hydrodynamics—A Meshfree Particle Method, World Scientific, 2003.
[26] P. Lancaster, K. Salkauskas, Surfaces by moving least squares methods, Mathematics of Computation 37 (155) (1981) 141–158.
[27] L. Rayleigh, On the capillary phenomena of jets, Proceedings of the Royal Society of London 29 (1879) 71.